Volume 14
Number 7
21 February 2023
Pages 1629–1922

Chemical Science

rsc.li/chemical-science

ISSN 2041-6539

ROYAL SOCIETY OF CHEMISTRY

EDGE ARTICLE
Steven H. L. Verhelst *et al.*
Azapeptide activity-based probes for the SARS-CoV-2 main protease enable visualization of inhibition in infected cells

Chemical Science

ROYAL SOCIETY OF CHEMISTRY

EDGE ARTICLE

View Article Online
View Journal | View Issue

Cite this: *Chem. Sci.*, 2023, **14**, 1666

All publication charges for this article have been paid for by the Royal Society of Chemistry

Azapeptide activity-based probes for the SARS-CoV-2 main protease enable visualization of inhibition in infected cells†

Roeland Vanhoutte, [a] Marta Barniol-Xicota, [a] Winston Chiu,[b] Laura Vangeel,[b] Dirk Jochmans, [b] Steven De Jonghe,[b] Hadeer Zidane,[c] Haim M. Barr,[c] Nir London, [d] Johan Neyts[b] and Steven H. L. Verhelst *[ae]

The COVID-19 pandemic has revealed the vulnerability of the modern, global society. With expected waves of future infections by SARS-CoV-2, treatment options for infected individuals will be crucial in order to decrease mortality and hospitalizations. The SARS-CoV-2 main protease is a validated drug target, for which the first inhibitor has been approved for use in patients. To facilitate future work on this drug target, we designed a solid-phase synthesis route towards azapeptide activity-based probes that are capped with a cysteine-reactive electrophile for covalent modification of the active site of M^{pro}. This design led to the most potent ABP for M^{pro} and one of the most potent inhibitors reported thus far. We demonstrate that this ABP can be used to visualize M^{pro} activity and target engagement by drugs in infected cells.

Received 25th July 2022
Accepted 2nd January 2023

DOI: 10.1039/d2sc04147b

rsc.li/chemical-science

Introduction

The SARS-CoV-2 virus is the causative agent of COVID-19 and has resulted in the largest worldwide viral pandemic in a century. The virus belongs to the family of betacoronaviruses, which have been known to infect humans since 1966[1,2] and have caused two previous pandemics: the SARS pandemic in 2002 [3] and the MERS pandemic in 2012.[4] Although the development of vaccines has lowered the incidence of hospitalizations and fatalities due to COVID-19, new mutants of the virus have been emerging for which the vaccines are less effective.[5] Despite the lower disease severity of the new mutants,[6] the infectivity has increased. As a result, future waves of infection with associated hospitalizations, hygienic measures and general societal burden are expected. Therefore, the development of antiviral drugs remains necessary in the battle against SARS-CoV-2.

The main protease (M^{pro}) of SARS-CoV-2 has gained a lot of attention as a drug target, as it is responsible for the proteolytic release of twelve of the sixteen non-structural proteins (nsps) from the two polyproteins expressed by the virus.[7] A wide variety of studies has therefore been conducted to generate inhibitors for M^{pro}, many of which employ compounds that bear cysteine-reactive warheads.[8,9] Various reversible covalent inhibitors have been reported. For example, Zhang *et al.* found that a previously discovered substrate-based inhibitor with an α-ketoamide warhead for alpha- and betacoronavirus M^{pro} and enterovirus 3C proteases was active against SARS-CoV-2 M^{pro}.[10] Similar substrate-based peptide aldehydes were reported around the same time as potent SARS-CoV-2 M^{pro} inhibitors.[11] GC376, a bisulfite adduct of a peptide aldehyde with a similar peptide sequence, which had already been developed as a prodrug against the feline coronavirus, also turned out to be potent against SARS-CoV-2 M^{pro}.[12,13] In December 2021, the FDA approved Pfizer's reversible covalent peptide nitrile nirmatrelvir[14] as a combination therapy with ritonavir, for the treatment of COVID-19.

Irreversible covalent inhibitors for M^{pro} have been reported based on various cysteine-reactive warheads, including acyloxy methyl ketones (AOMKs),[15] azanitriles and pyridyl esters,[16] and Michael acceptors such as peptide vinyl esters[17] and vinyl sulfones.[18] Additionally, some covalent drugs or drug candidates, such as carmofur and ebselen, were reported as SARS-CoV-2 M^{pro} inhibitors.[17]

[a]*Department of Cellular and Molecular Medicine, Laboratory of Chemical Biology, KU Leuven, Herestraat 49 box 802, 3000 Leuven, Belgium. E-mail: steven.verhelst@kuleuven.be*

[b]*Laboratory of Virology and Chemotherapy, Department of Microbiology, Immunology and Transplantation, Rega Institute for Medical Research, KU Leuven, Herestraat 49, Box 1043, 3000, Leuven, Belgium*

[c]*Maurice and Vivienne Wohl Institute for Drug Discovery, The Nancy and Stephen Grand Israel National Center for Personalized Medicine, The Weizmann Institute of Science, Rehovot 7610001, Israel*

[d]*Department of Chemical and Structural Biology, Weizmann Institute of Science, Rehovot 7610001, Israel*

[e]*AG Chemical Proteomics, Leibniz Institute for Analytical Sciences ISAS, Otto-Hahn-Str. 6b, 44227 Dortmund, Germany*

† Electronic supplementary information (ESI) available. See DOI: https://doi.org/10.1039/d2sc04147b

Several irreversible covalent warheads have been used to create activity-based probes (ABPs) for M^{pro}. Rut *et al.* used a vinyl sulfone warhead attached to a tetrapeptide containing natural and unnatural amino acids optimized for the P_4–P_1 preference of M^{pro}, with a fluorophore or biotin detection tag.[18] The group of Böttcher created M^{pro}-reactive ABPs in a library synthesis by coupling an amine-containing ligand with a chloroacetamide-containing activated ester.[19] Although the above studies provided useful probes, both used solution-phase chemistry for the construction of these molecules. Solid-phase chemistry would allow creation of a larger variety of structures in a shorter time. Van de Plassche *et al.* implemented solid-phase peptide synthesis (SPPS) to create ABPs with an AOMK warhead.[20] However, this solid-phase approach is restricted to this particular warhead. Therefore, we aimed at designing a solid-phase strategy that would allow variation of the peptidic element as well as the reactive warhead. In this work, we report the on-resin synthesis of azapeptide-derived ABPs and their application in visualizing M^{pro} activity and inhibition in infected cells.

Results & discussion

For our synthetic design, we aimed at using a SPPS-based method that does not only allow rapid synthesis, but also enables the introduction of the reactive electrophilic warhead in a last step for easy diversification of this essential element of the ABP. Of note, cysteine-reactive electrophiles span a wide range of reactivities,[21–23] and finding the right reactivity may be crucial to obtain an optimal ABP. In addition, not all electrophiles may be compatible with peptide elongation conditions. Coupling the electrophile in a final step is therefore highly desirable. Conveniently, the primary specificity element of SARS-CoV-2 M^{pro} comprises a Gln residue in the P_1 position (Fig. 1A), which opens the possibility to anchor the molecule to the solid support at this position. As the warhead is placed at the C-terminal end of the P_3–P_1 peptide recognition element, we opted for the use of an azapeptide, introducing a secondary nitrogen in the peptide backbone to which a warhead can be coupled (Fig. 1B). Covalent azapeptidic inhibitors were previously developed for various cysteine proteases, including caspases[24] and M^{pro} of the SARS-CoV-1 virus, which emerged in 2002.[25] Recently, a covalent inhibitor of the SARS-CoV-2 papain-like protease based on an azaglycine-type scaffold has also been reported.[26] In addition, we have previously provided proof of principle that solid-phase synthesis is possible for caspase-targeting inhibitors with a P_1 aza-Asp residue.[27,28]

Initially, we aimed at constructing the azapeptide completely on a solid support by coupling bromopropionate to Rink resin, followed by reaction with Fmoc-hydrazine (Scheme 1A). The substitution unfortunately failed, likely due to the low nucleophilicity of Fmoc-hydrazine and the substantially lower electrophilicity of the bromopropionate compared with bromoacetate, for which substitution can be readily achieved.[27] Performance of this reaction in solution-phase synthesis also failed, supporting this explanation (Scheme 1B). To enable SPPS of the desired azapeptides, we therefore constructed key building block **4** in solution, starting from Boc-protected hydrazine and *tert*-butyl 3-bromopropanoate (Scheme 1C), which was reported to proceed in better yields than for Fmoc-hydrazine.[29] After the substitution, the N^1 was protected using Alloc chloride to give intermediate **3**, from which both the Boc and *tert*-butyl ester were removed using HCl. Finally, the N^2 was reprotected with Fmoc chloride to form P_1 building block **4**.

Compound **4** represents the cornerstone for the on-resin synthesis of the ABPs, as it serves a threefold purpose: the

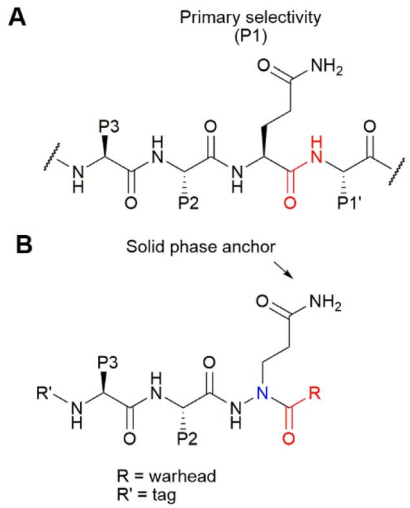

Fig. 1 (A) Substrates of M^{pro} contain a Gln residue in the P_1 position, directly N-terminal to the scissile bond (in red). (B) Design of azapeptide ABPs. The Gln side chain serves as a solid-phase anchor. It is introduced as an aza-amino acid, in which the α-carbon is replaced by nitrogen (blue). The aza-amino acid can then be capped with a cysteine-reactive warhead. The detection tag at the N-terminus allows detection of the covalent probe–M^{pro} complex.

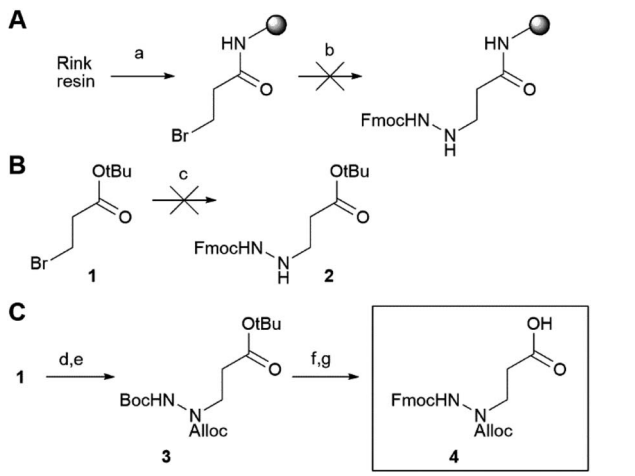

Scheme 1 Synthesis of the azapeptide building block. (A) An attempt to synthesize a P_1 azaGln fragment on a Rink amide resin did not work. (a) 3-Bromo propionyl bromide, DIEA, and DCM. (b) Fmoc-hydrazine, DIEA, DMF, 40 °C. (B) In solution, substitution by Fmoc-hydrazine did not function. (c) Fmoc-hydrazine, DIEA, DMF, 40 °C. (C) Synthesis of central orthogonally protected building block **4**, (d) Boc-hydrazine, DIEA, DMF, 40 °C. (e) Alloc-Cl, DIEA, DMF, rt, 26% over two steps. (f) TFA, DCM, rt. (g) Fmoc-Cl, DIEA, DCM, rt, 69% over two steps.

anchor point to the resin, the site for attachment of the peptide recognition element and the position for connection of the warhead. Building block **4** was first coupled to Rink amide resin *via* its carboxylic acid function, yielding the desired Gln side chain attached to the solid support. Next, we used Fmoc-based SPPS to couple an L-Leu and L-Tle residue to the N^2 of the P_1 azapeptide element. After capping the peptide with a hexynoic acid alkyne tag, the Alloc on the N^1 was removed and capped with a cysteine-reactive warhead. We installed five different reactive electrophiles *via* an amide or sulfonamide bond: an epoxysuccinate (**7a**), a vinylsulfonamide (**7b**), a methylfumarate (**7c**), a chloroacetamide (**7d**) and a 2-chloro-5-nitrobenzamide (**7e**). These warheads react with cysteines in four different ways, namely epoxide ring opening (**7a**), Michael addition (**7b** and **7c**), S_N2 substitution (**7d**) and S_NAr substitution (**7e**). After coupling of the warheads, the probes were cleaved from the resin using a mixture of TFA, TIS and water, which was compatible with all warheads installed on the probes (Scheme 2).

A first assessment of the probes was done by competitive activity-based protein profiling (ABPP). Herein, M^{pro} was pre-treated with **7a–e** and residually active enzyme was labeled with the previously reported[20] TAMRA-Tle-Leu-Gln-AOMK probe. At 10 μM concentration, probes **7a**, **7c** and **7d** showed strong inhibition of M^{pro}, whereas probes **7b** and **7e** showed none or little (Fig. S1†). Next, apparent IC_{50} values (IC_{50}^{App}) were determined with a kinetic assay using a quenched fluorescent substrate. This revealed a large difference in activity between the probes. While probes **7a**, **7c** and **7d** display low-to-mid nanomolar IC_{50}^{App}, **7b** and **7e** are much less active with IC_{50}^{App} values exceeding 45 μM (Table 1). This difference in activity is striking, as the vinyl sulfone warhead of **7b** is the strongest Cys-reactive warhead used in this study.[21] A potential explanation lies in the distance between the site of attack of the nucleophilic Cys residue on the warhead and the α-position of the P_1 residue. For probes **7a**, **7c** and **7d**, this distance is two

Table 1 Activity of **7a–e** on purified SARS-CoV-2 M^{pro} and infected cells

Compound	IC_{50}^{App} [a]	EC_{50} [b]	CC_{50} [c]	CC_{50} [d]
7a	206 nM	>10 μM	36.7 μM	N.D.
7b	Inactive	N.D.	N.D.	N.D.
7c	44.0 nM	>10 μM	62.5 μM	N.D.
7d	20.8 nM	3.25 μM	50.0 μM	>10 μM
7e	>45 μM	N.D.	N.D.	N.D.

[a] Measured on purified SARS-CoV-2 M^{pro}. [b] Measured on VeroE6 cells infected with SARS-CoV-2. [c] Measured on Huh7 cells. [d] Measured on VeroE6 cells.

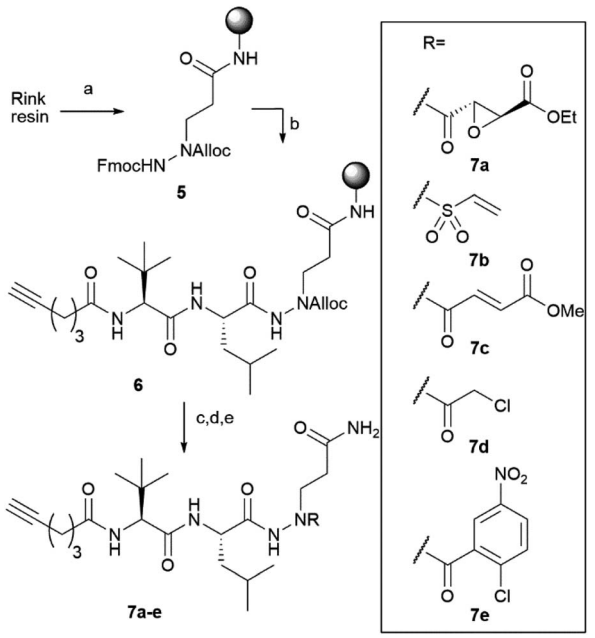

Scheme 2 On-resin synthesis of ABPs **7a–e**. (a) (1) Deprotection with DMF/piperidine 4/1; (2) **4**, HBTU, DIEA, DMF, rt, overnight. (b) Elongation by repeated cycles of: (1) DMF/piperidine 4/1, 5 minutes; (2) Fmoc-Leu-OH (overnight), Fmoc-Tle-OH or hexynoic acid (3 h), HBTU, DIEA, DMF, rt. (c) $Pd(PPh_3)_4$, $PhSiH_3$, DCM, 30 minutes. (d) Coupling of either: (1) mono-ethyl epoxysuccinate, HBTU, DIEA, DMF, rt, overnight; (2) 2-chloroethane sulfonylchloride, DIEA, DCM, rt, overnight; (3) mono-methyl fumarate, HBTU, DIEA, DMF, rt, overnight; (4) chloroacetyl chloride, DIEA, DCM, rt, overnight; or (5) 2-chloro-5-nitrobenzoic acid, HBTU, DIEA, DMF, rt, overnight. (e) TFA/TIS/water 95/2.5/2.5, 30 minutes.

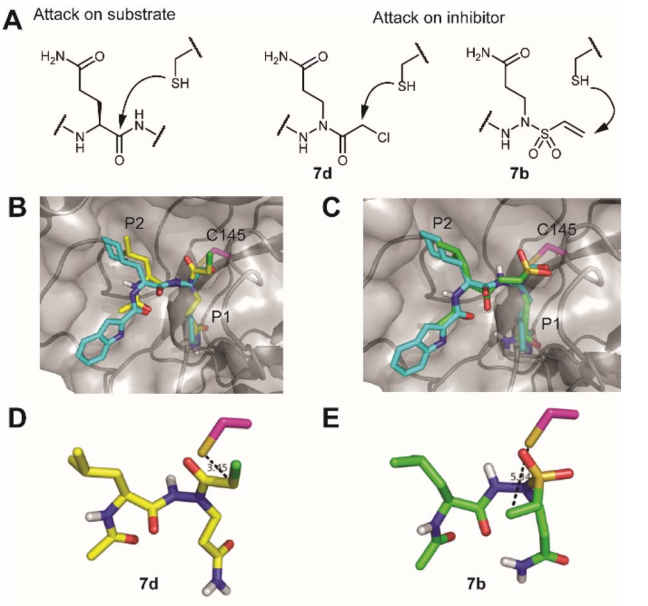

Fig. 2 Engagement of the warhead by the active site cysteine. (A) Comparison of the position of attack on a substrate *versus* the here-synthesized inhibitors with chloroacetamide (**7d**) and vinylsulfonamide (**7b**). (B) Overlay of the crystal structure of SARS-CoV-2 M^{pro} with an aldehyde inhibitor (PDB code: 6LZE) with a docked structure of a vinylsulfonamide. M^{pro} is depicted as a semitransparent surface with a protein backbone in a cartoon format. Active site cysteine C145 is colored in magenta, the original inhibitor in cyan and the docked structure in green. (C) Overlay of the same crystal structure with a docked structure of a chloroacetamide. (D) Position of the vinylsulfonamide relative to the active site cysteine. Note that the electrophilic carbon points away from the nucleophile. (E) Position of the chloroacetamide relative to the active site cysteine. Pictures were rendered in PyMol.[30]

bonds, whereas for probes **7b** and **7e**, this is three bonds (Fig. 2A). It would thus appear that the two-bond distance is a strict requirement for this type of M^{pro} inhibitor to engage in a productive reaction with the active site cysteine, although a larger number of warheads should be tested to confirm this hypothesis. To gain some more insight into the difference in reactivity, the warhead, P_1 and P_2 residues of the most active compound **7d** and the inactive vinylsulfonamide **7b** were docked into the active site of M^{pro}. The top docking poses that displayed good overlap with a known peptidic M^{pro} inhibitor (Fig. 2B and C), showed that the electrophilic carbon of the chloroacetamide is in close distance of the active site C145, whereas the vinyl moiety of **7b** is localized much further and points towards the opposite direction (Fig. 2D and E).

Next, the selectivity of probes **7a**, **7c**, **7d** and **7e** for M^{pro} over human proteins was assessed in a whole proteome by ABPP. To this end, HEK293 lysates were spiked with M^{pro} and treated with a 1 μM probe concentration. Covalently modified probe targets were then visualized *via* CuAAC (copper(I)-catalyzed azide alkyne cycloaddition) with TAMRA-azide. At pH 7.5, which is around the optimal pH for M^{pro}, we detected only one gel band for probes **7a**, **7c** and **7d**. Compound **7e** did not yield any signal, further confirming its inactivity. The fluorescent gel band was identified as M^{pro}, as it corresponds to the right molecular mass of the protein and the same band was detected when using the known M^{pro}-reactive ABP TAMRA-Tle-Leu-Gln-AOMK on HEK-lysates spiked with wild type M^{pro}, but not when the lysate was spiked with a catalytically dead C145A M^{pro} mutant. Because various reported covalent M^{pro} inhibitors show cross reactivity with cysteine cathepsins,[15,16,31] the same experiment was also performed at pH 5.5, which is the optimal pH for cysteine cathepsin proteases. The occurrence of cathepsins in HEK-lysates was confirmed by using fluorescently labelled DCG-04, a pan-reactive cathepsin ABP.[32] None of the probes (**7a**, **7c**, **7d** and **7e**) showed any protein labelling at this pH (other than M^{pro}), illustrating the lack of off-targets. Striking was the clear labeling of M^{pro} by **7c** and **7d** at this acidic pH, showcasing the strong reactivity of these probes, even under sub-optimal conditions.

We next assessed the sensitivity of the two most active probes, **7c** and **7d** for labelling M^{pro}. To this end, 20 nM M^{pro} was incubated with decreasing concentrations of ABP and visualized *via* CuAAC with TAMRA-azide. Probe **7c** gave a detectable M^{pro} signal down to 42 nM concentration and probe **7d** detected M^{pro} even at a substoichiometric probe concentration of 14 nM (Fig. S2A†). The detection limit of probe **7d** was also determined in a whole proteome by spiking HEK293T lysates (1 mg mL^{-1} total protein) with decreasing amounts of M^{pro}. With 1 μM **7d**, it was possible to detect active M^{pro} down to 0.05% of the total protein (Fig. S2B†). This suggests that probe **7d** may be used to detect active M^{pro} in infected cells.

With these highly active and selective probes at hand, we now set out to detect M^{pro} activity and its inhibition in infected cells. First, we determined the capacity of probes **7a**, **7c** and **7d** to inhibit SARS-CoV-2 replication in VeroE6 cells. Compounds **7a** and **7c** showed low potency (EC_{50} > 10 μM), while compound

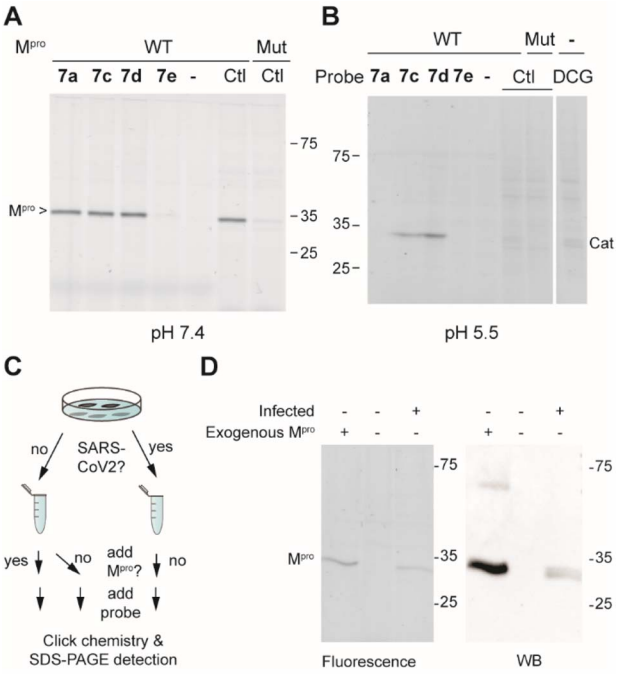

Fig. 3 (A) Labeling of M^{pro}-spiked HEK lysates (1 mg mL; 0.1% M^{pro}) at pH 7.5 with probes **7a**, **7c**, **7d** and **7e** (1 μM for 1 h) with visualization *via* CuAAC with TAMRA-N_3. Mut = C145A active site M^{pro} mutant and Ctl = control M^{pro} probe TAMRA-Tle-Leu-Gln-AOMK, which labels the active M^{pro} but not the catalytically dead mutant. (B) Same as in panel (A), but at pH 5.5. DCG = TAMRA-conjugated DCG-04 pan cathepsin probe. (C) Schematic workflow of M^{pro} detection in samples of infected and uninfected cells. (D) Detection of M^{pro} that is fluorescently labeled by probe **7d** (left panel) and of total M^{pro} by western blot (right panel).

7d displayed single digit micromolar activity. The cellular toxicity (CC_{50}) of all compounds was in the mid-micromolar range (Table 1). To illustrate that probe **7d** can detect endogenous levels of M^{pro}, SARS-CoV-2-infected cells were lysed and treated with **7d**. As controls, lysates of non-infected cells with or without spiked exogenous recombinant M^{pro} were treated under the same conditions (Fig. 3C). A fluorescently-labeled band was only visible in the sample from infected cells as well as in the spiked sample, whereas not a single fluorescent band was observed in the non-infected sample (Fig. 3D), confirming the high probe selectivity seen in Fig. 3A and B. The presence of M^{pro} was confirmed by western blot, which revealed distinct bands that overlay with the fluorescently-labeled bands of probe detection (Fig. 3D).

With the ability to label endogenous M^{pro}, the most effective azapeptide ABP **7d** was now used for detection of M^{pro} activity in virally infected cells by fluorescence microscopy. Hence, VeroE6 cells were incubated with SARS-CoV-2 for 24 h, followed by a 2 h treatment with an M^{pro} inhibitor or a DMSO vehicle. Next, ABP **7b** (10 μM) was added to detect residually active M^{pro}. Labeled M^{pro} was then visualized after cell fixation by CuAAC with TAMRA-azide, whereas presence of the virus was detected with an antibody against the SARS-CoV-2 nucleocapsid protein. Samples were subjected to automated fluorescence microscopy

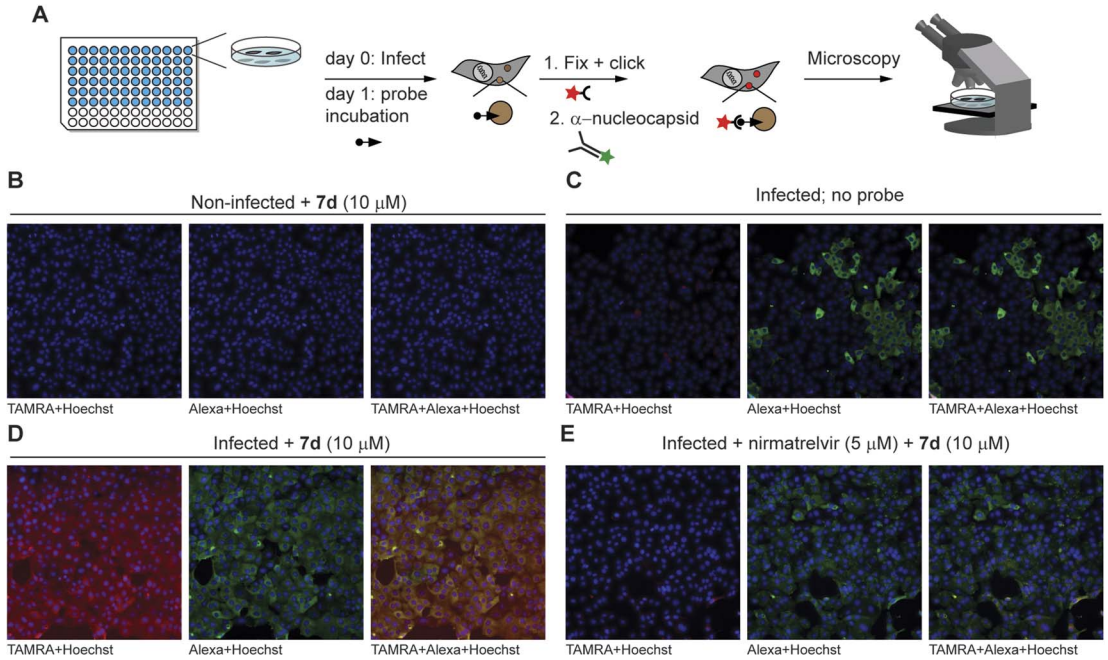

Fig. 4 Fluorescence microscopy detection of M^{pro} inhibition in SARS-CoV-2-infected cells. (A) Summary of workflow. One day after infection of VeroE6 cells, probes were added to cells – with or without inhibitor pretreatment. Click chemistry with TAMRA-N_3 as well as antibody staining against the nucleocapsid protein of the virus were performed after fixation, followed by fluorescence microscopy. The minimum intensity for visualization was set above the background intensity of no probe control samples. (B) Non-infected control cells do not show TAMRA staining derived from the probe (in red) or Alexa647 staining of the SARS-CoV-2 anti-nucleocapsid protein (in green). (C) Infected cells without probe treatment do not show red fluorescence in the cells positive for the SARS-CoV-2 virus (green). (D) Treatment with probe **7d** results in red staining of infected cells, which can be seen by yellow co-staining in the overlay panel. The staining can be attributed to M^{pro} activity, as uninfected cells (panel (B)) and cells not treated with the probe (panel (C)) do not show this. (E) M^{pro} inhibitor nirmatrelvir reduces the signal by probe **7d**, further indicating that **7d** reacts with active M^{pro}. See Fig. S4† for overlay channels and bright light images of cells.

with a ThermoFisher ArrayScan XTI system (Fig. 4A). Non-infected cells showed a low probe-derived TAMRA signal and low Alexafluor 647-derived signal of the viral nucleocapsid protein, indicating high selectivity of the *in situ* click reaction and the antibody, respectively (Fig. 4B). Infected cells not treated with probe **7b** also displayed low TAMRA fluorescence, further confirming the *in situ* click selectivity (Fig. 4C). In contrast, virus-infected cells were well visualized by using probe **7d** as demonstrated by the red fluorescence, which overlays with the false-green colored antibody fluorescence (Fig. 4D). Importantly, the probe signal disappeared almost completely in cells treated with nirmatrelvir (Fig. 4E and S3–S4†) as well as with carmofur (Fig. S3†), an antineoplastic drug that also inhibits SARS-CoV-2 M^{pro}. Although the fluorescence was relatively weak compared with the background, quantification of the signal shows a reduction in the fluorescence of nirmatrelvir-treated cells to levels close to the background (Fig. S5†). This confirms that the fluorescence signal indeed stems from the reaction of active M^{pro} with probe **7d** and demonstrates the utility in detection of this viral drug target and its inhibition in live cells.

Conclusions

M^{pro} is an essential enzyme for SARS-CoV-2 replication and therefore represents an attractive drug target. To enable the detection of active M^{pro} within infected cells, here we developed highly potent and selective ABPs. A multifunctional design of azapeptide building block **4** allowed solid-phase synthesis and rapid variation of the reactive electrophile, which is a crucial element of ABPs. We found that azapeptide chloroacetamide **7d** was highly active against SARS CoV-2 M^{pro} in a biochemical assay. This type of reactive warhead had a large influence on the potency of inhibition. Interestingly, the vinyl sulfonamide derivative, an electrophile with the highest reported reactivity, was inactive, likely because of the unfavorable placement in relation to the nucleophilic cysteine in the active site. Although compound **7d** has high potency *in vitro*, the activity in cells is substantially lower, which is likely due to poor cell permeability. This can be attributed to the primary amide that mimics the glutamine side chain, as a related azapeptide inhibitor with a pyrrolidone as a cyclic glutamine side chain analog, reported during the course of this work, displays nanomolar potency.[33] We therefore expect that the cellular potency of the here-reported probes, and thereby the applicability in cells, can be further fine-tuned by optimization of the peptide element as well as the reactive group. In this regard, the recent discovery of di- and trihaloacetamides as reactive electrophiles for SARS-CoV-2 M^{pro} may also be useful for future design of novel azapeptide M^{pro} inhibitors and probes.[34] The solid-phase method described here will enable rapid synthesis of libraries of such compounds. Additionally, variation of the P_1 position and the reactive warhead may also facilitate the development of ABPs

for other viral proteases. The here-reported probe **7d** permits the visualization of drug target engagement in a cellular context. We expect that this may aid future drug discovery efforts directed towards SARS-CoV-2 M^{pro}.

Data availability

The coordinates of the docked compounds are available from the Research Data Repository of KU Leuven at: **https://www.rdr.kuleuven.be**.

Author contributions

RV and SV conceived the project, RV performed chemical synthesis and biochemical evaluation, MBX performed protein expression and biochemical evaluation, WC performed experiments with the live virus, HZ and HMB performed IC_{50} measurements, SV performed *in silico* docking and mutagenesis, SV, NL, LV, DJ, SDJ, and JN supervised the experiments, and RV and SV performed data analysis and wrote the paper. All authors have given approval to the final version of the manuscript.

Conflicts of interest

The authors declare no conflicts of interest.

Acknowledgements

We thank Rita Derua for help in recording HRMS, Luc Baudemprez for NMR, Joost Schepers, Tina Van Buyten and Thibault Francken for assistance with SARS-CoV-2 assays, and the COVID Moonshot consortium for contributing reagents. We acknowledge financial support from KU Leuven (PDM grant PDMT2/21/074 to RV), Research Foundation Flanders FWO (project no. G0E3617N and post-doc fellowship 12A2723N), the Ministerium für Kultur und Wissenschaft des Landes Nordrhein-Westfalen, the Regierende Bürgermeister von Berlin, and the Bundesministerium für Bildung und Forschung. Part of this research work was performed using the 'Caps-It' research infrastructure (project ZW13-02) that was financially supported by the Hercules Foundation, Belgium and Rega Foundation, KU Leuven.

Notes and references

1 D. A. Tyrrell and M. L. Bynoe, *Lancet*, 1966, **1**, 76–77.
2 D. Hamre and J. J. Procknow, *Proc. Soc. Exp. Biol. Med.*, 1966, **121**, 190–193.
3 T. Kuiken, R. A. M. Fouchier, M. Schutten, G. F. Rimmelzwaan, G. Van Amerongen, D. Van Riel, J. D. Laman, T. De Jong, G. Van Doornum, W. Lim, A. E. Ling, P. K. S. Chan, J. S. Tam, M. C. Zambon, R. Gopal, C. Drosten, S. Van Der Werf, N. Escriou, J. C. Manuguerra, K. Stöhr, J. S. M. Peiris and A. D. M. E. Osterhaus, *Lancet*, 2003, **362**, 263–270.
4 A. M. Zaki, S. van Boheemen, T. M. Bestebroer, A. D. M. E. Osterhaus and R. A. M. Fouchier, *N. Engl. J. Med.*, 2012, **367**, 1814–1820.
5 H. F. Tseng, B. K. Ackerson, Y. Luo, L. S. Sy, C. A. Talarico, Y. Tian, K. J. Bruxvoort, J. E. Tubert, A. Florea, J. H. Ku, G. S. Lee, S. K. Choi, H. S. Takhar, M. Aragones and L. Qian, *Nat. Med.*, 2022, **28**, 1063–1071.
6 A. Sigal, R. Milo and W. Jassat, *Nat. Rev. Immunol.*, 2022, **22**, 267–269.
7 S. Ullrich and C. Nitsche, *Bioorg. Med. Chem. Lett.*, 2020, **30**, 127377.
8 H. Yang and J. Yang, *RSC Med. Chem.*, 2021, **12**, 1026–1036.
9 C. S. B. Chia, W. Xu and P. Shuyi Ng, *ChemMedChem*, 2022, **17**, e202100576.
10 L. Zhang, D. Lin, X. Sun, U. Curth, C. Drosten, L. Sauerhering, S. Becker, K. Rox and R. Hilgenfeld, *Science*, 2020, **368**, 409–412.
11 W. Dai, B. Zhang, X. M. Jiang, H. Su, J. Li, Y. Zhao, X. Xie, Z. Jin, J. Peng, F. Liu, C. Li, Y. Li, F. Bai, H. Wang, X. Cheng, X. Cen, S. Hu, X. Yang, J. Wang, X. Liu, G. Xiao, H. Jiang, Z. Rao, L. K. Zhang, Y. Xu, H. Yang and H. Liu, *Science*, 2020, **368**, 1331–1335.
12 W. Vuong, M. B. Khan, C. Fischer, E. Arutyunova, T. Lamer, J. Shields, H. A. Saffran, R. T. McKay, M. J. van Belkum, M. A. Joyce, H. S. Young, D. L. Tyrrell, J. C. Vederas and M. J. Lemieux, *Nat. Commun.*, 2020, **11**, 5409.
13 C. Ma, M. D. Sacco, B. Hurst, J. A. Townsend, Y. Hu, T. Szeto, X. Zhang, B. Tarbet, M. T. Marty, Y. Chen and J. Wang, *Cell Res.*, 2020, **30**, 678–692.
14 D. R. Owen, C. M. N. Allerton, A. S. Anderson, L. Aschenbrenner, M. Avery, S. Berritt, B. Boras, R. D. Cardin, A. Carlo, K. J. Coffman, A. Dantonio, L. Di, H. Eng, R. A. Ferre, K. S. Gajiwala, S. A. Gibson, S. E. Greasley, B. L. Hurst, E. P. Kadar, A. S. Kalgutkar, J. C. Lee, J. Lee, W. Liu, S. W. Mason, S. Noell, J. J. Novak, R. S. Obach, K. Ogilvie, N. C. Patel, M. Pettersson, D. K. Rai, M. R. Reese, M. F. Sammons, J. G. Sathish, R. S. P. Singh, C. M. Steppan, A. E. Stewart, J. B. Tuttle, L. Updyke, P. R. Verhoest, L. Wei, Q. Yang and Y. Zhu, *Science*, 2021, **374**, 1586–1593.
15 B. Bai, A. Belovodskiy, M. Hena, A. S. Kandadai, M. A. Joyce, H. A. Saffran, J. A. Shields, M. B. Khan, E. Arutyunova, J. Lu, S. K. Bajwa, D. Hockman, C. Fischer, T. Lamer, W. Vuong, M. J. Van Belkum, Z. Gu, F. Lin, Y. Du, J. Xu, M. Rahim, H. S. Young, J. C. Vederas, D. L. Tyrrell, M. J. Lemieux and J. A. Nieman, *J. Med. Chem.*, 2022, **65**, 2905–2925.
16 J. Breidenbach, C. Lemke, T. Pillaiyar, L. Schäkel, G. Al Hamwi, M. Diett, R. Gedschold, N. Geiger, V. Lopez, S. Mirza, V. Namasivayam, A. C. Schiedel, K. Sylvester, D. Thimm, C. Vielmuth, L. Phuong Vu, M. Zyulina, J. Bodem, M. Gütschow and C. E. Müller, *Angew. Chem., Int. Ed.*, 2021, **60**, 10423–10429.
17 Z. Jin, X. Du, Y. Xu, Y. Deng, M. Liu, Y. Zhao, B. Zhang, X. Li, L. Zhang, C. Peng, Y. Duan, J. Yu, L. Wang, K. Yang, F. Liu, R. Jiang, X. Yang, T. You, X. Liu, X. Yang, F. Bai, H. Liu, X. Liu, L. W. Guddat, W. Xu, G. Xiao, C. Qin, Z. Shi, H. Jiang, Z. Rao and H. Yang, *Nature*, 2020, **582**, 289–293.

18 W. Rut, K. Groborz, L. Zhang, X. Sun, M. Zmudzinski, B. Pawlik, X. Wang, D. Jochmans, J. Neyts, W. Młynarski, R. Hilgenfeld and M. Drag, *Nat. Chem. Biol.*, 2021, **17**, 222–228.

19 L. Peñalver, P. Schmid, D. Szamosvári, S. Schildknecht, C. Globisch, K. Sawade, C. Peter and T. Böttcher, *Angew. Chem., Int. Ed.*, 2021, **60**, 6799–6806.

20 M. A. T. van de Plassche, M. Barniol-Xicota and S. H. L. Verhelst, *ChemBioChem*, 2020, **21**, 3383–3388.

21 J. S. Martin, C. J. MacKenzie, D. Fletcher and I. H. Gilbert, *Bioorg. Med. Chem.*, 2019, **27**, 2066–2074.

22 E. Resnick, A. Bradley, J. Gan, A. Douangamath, T. Krojer, R. Sethi, P. P. Geurink, A. Aimon, G. Amitai, D. Bellini, J. Bennett, M. Fairhead, O. Fedorov, R. Gabizon, J. Gan, J. Guo, A. Plotnikov, N. Reznik, G. F. Ruda, L. Díaz-Sáez, V. M. Straub, T. Szommer, S. Velupillai, D. Zaidman, Y. Zhang, A. R. Coker, C. G. Dowson, H. M. Barr, C. Wang, K. V. M. Huber, P. E. Brennan, H. Ovaa, F. Von Delft and N. London, *J. Am. Chem. Soc.*, 2019, **141**, 8951–8968.

23 L. Petri, P. Ábrányi-Balogh, P. R. Varga, T. Imre and G. M. Keserű, *Bioorg. Med. Chem.*, 2020, **28**, 115357.

24 J. L. Asgian, K. E. James, Z. Z. Li, W. Carter, A. J. Barrett, J. Mikolajczyk, G. S. Salvesen and J. C. Powers, *J. Med. Chem.*, 2002, **45**, 4958–4960.

25 T. W. Lee, M. M. Cherney, C. Huitema, J. Liu, K. E. James, J. C. Powers, L. D. Eltis and M. N. G. James, *J. Mol. Biol.*, 2005, **353**, 1137–1151.

26 B. Sanders, S. Pohkrel, A. Labbe, I. Mathews, C. Cooper, R. Davidson, G. Phillips, K. Weiss, Q. Zhang, H. O'Neill, M. Kaur, L. Ferrins, J. Schmidt, W. Reichard, S. Surendranathan, D. Kumaran, B. Andi, G. Babnigg, N. Moriarty, P. Adams, A. Joachimiak, C. Jonsson, S. Wakatsuki, S. Galanie, M. Head and J. Parks, *Res. Sq.*, 2022, rs.3.rs-1840200.

27 D. Kato, S. H. L. Verhelst, K. B. Sexton and M. Bogyo, *Org. Lett.*, 2005, **7**, 5649–5652.

28 K. B. Sexton, D. Kato, A. B. Berger, M. Fonovic, S. H. L. Verhelst and M. Bogyo, *Cell Death Differ.*, 2007, **14**, 727–732.

29 O. Busnel and M. Baudy-Floc'h, *Tetrahedron Lett.*, 2007, **48**, 5767–5770.

30 W. L. Delano, *The PyMol Molecular Graphics System*, **https://www.pymol.org**.

31 K. Steuten, H. Kim, J. C. Widen, B. M. Babin, O. Onguka, S. Lovell, O. Bolgi, B. Cerikan, C. J. Neufeldt, M. Cortese, R. K. Muir, J. M. Bennett, R. Geiss-Friedlander, C. Peters, R. Bartenschlager and M. Bogyo, *ACS Infect. Dis.*, 2021, **7**, 1457–1468.

32 D. Greenbaum, A. Baruch, L. Hayrapetian, Z. Darula, A. Burlingame, K. F. Medzihradszky and M. Bogyo, *Mol. Cell. Proteomics*, 2002, **1**, 60–68.

33 Y. Hirose, N. Shindo, M. Mori, S. Onitsuka, H. Isogai, R. Hamada, T. Hiramoto, J. Ochi, D. Takahashi, T. Ueda, J. M. M. Caaveiro, Y. Yoshida, S. Ohdo, N. Matsunaga, S. Toba, M. Sasaki, Y. Orba, H. Sawa, A. Sato, E. Kawanishi and A. Ojida, *J. Med. Chem.*, 2022, **65**, 13852–13865.

34 C. Ma, Z. Xia, M. D. Sacco, Y. Hu, J. A. Townsend, X. Meng, J. Choza, H. Tan, J. Jang, M. V. Gongora, X. Zhang, F. Zhang, Y. Xiang, M. T. Marty, Y. Chen and J. Wang, *J. Am. Chem. Soc.*, 2021, **143**, 20697–20709.